On the relationship between oxygen K edge fine structure and cobalt/nickel content in magnetite-based core-shell nanoparticles☆

Simon Hettler [a,b,c,*], Raul Arenal [b,c,d]

[a] Laboratorium für Elektronenmikroskopie, Karlsruhe Institut für Technologie, Karlsruhe, Germany
[b] Instituto de Nanociencia y Materiales de Aragón (INMA), CSIC-Universidad de Zaragoza, Zaragoza, Spain
[c] Laboratorio de Microscopías Avanzadas (LMA), Universidad de Zaragoza, Zaragoza, Spain
[d] ARAID Foundation, Zaragoza, Spain

ARTICLE INFO

ABSTRACT

Iron oxide nanoparticles (NPs) are used in a broad range of applications and offer the possibility of fine tuning their properties by forming hybrid core-shell structures. Scanning transmission electron microscopy (STEM) combined with electron energy loss spectroscopy (EELS) is frequently used to study such NPs at the local scale. Specifically, the energy loss near edge structure (ELNES) provides rich information on the local chemistry. Here, the dependence between the ELNES signal of the oxygen K edge and the incorporation of cobalt and nickel into the shell of magnetite NPs is investigated quantitatively using an intensity ratio between specific energy windows of the O-K edge. The analysis shows that both the local and global cobalt and nickel content of a NP influence this relationship. In addition, the overlap between the Fe-L_1 and Ni-$L_{2,3}$ edges is studied, the impact of a supporting film on the ELNES analysis is discussed, and the importance of a clean sample preparation is demonstrated.

1. Introduction

Iron oxide nanoparticles (NPs) are of interest for a wide range of applications due to their controllable magnetic and electronic properties, high biocompatibility, facile synthesis, and high natural abundance (Tartaj et al., 2011; Wallyn et al., 2019; Ajinkya et al., 2020; Bustamante Torres et al., 2022). They are also frequently applied as host NPs to form hybrid core-shell structures with the aim of tailoring magnetic properties or for catalytic purposes (Lima et al., 2012; López-Ortega et al., 2012,2015; Estrader et al., 2015; Sartori et al., 2020; Royer et al., 2022; Nuñez et al., 2022; Makarchuk et al., 2025). These works have shown that minute changes in shape or local composition can have strong effects on the macroscopic properties of NPs, requiring the detailed analysis of the structure and composition at high spatial resolution.

Transmission electron microscopy (TEM) and scanning (S)TEM in combination with electron energy-loss spectroscopy (EELS) can provide this information and have been frequently used in recent studies to analyze iron-oxide-based NPs (Turner et al., 2011; Lin et al., 2025; Gavrilov-Isaac et al., 2015; Sartori et al., 2021; Royer et al., 2023; Makarchuk et al., 2025). STEM-EELS, where the electron beam is scanned over the sample and an EEL spectrum is acquired at each beam

position, has gained importance compared to energy-filtered TEM (EFTEM) since aberration correctors have been developed. EELS not only gives access to the local composition, but the analysis of the shape and intensity distribution of the ionization edge structure, called energy loss near edge structure (ELNES), provides additional information on the local valence state and chemical environment. Many studies have been published on ELNES analysis of iron oxides focusing on the relationship between the valence of iron on one side and the shape and intensity distribution of the Fe-$L_{2,3}$ and O-K edges on the other side (Garvie and Buseck, 1998; van Aken et al., 1998; Mitterbauer et al., 2003; Chen et al., 2009; Tan et al., 2012). Similar studies exist for cobalt and nickel oxides (Potapov et al., 2001; Barreca et al., 2010). This ELNES information has been used to probe the local oxidation state in iron oxide and related NPs (Turner et al., 2011; Knappett et al., 2013; Lin et al., 2025; Torruella et al., 2016; López-Ortega et al., 2017; Gavrilov-Isaac et al., 2015; Roldan et al., 2021). Great effort has been put into the development of advanced data analysis techniques for STEM-EELS datasets to deal, among others, with experimental noise caused by beam damage limitations in small NP structures (Yedra et al., 2014; Blanco-Portals et al., 2021; Pate et al., 2025).

In this paper, the detailed STEM-EELS and ELNES analysis of a series

---

☆ This work is dedicated to the memory of Misa Hayashida.
* Corresponding author at: Laboratorium für Elektronenmikroskopie, Karlsruhe Institut für Technologie, Karlsruhe, Germany.
E-mail address: simon.hettler@kit.edu (S. Hettler).

of NPs based on magnetite iron oxide decorated with varying amounts of cobalt and nickel at their surface is presented. The impact of the overlap between the minor Fe-L$_1$ edge and the Ni-L$_{2,3}$ edge on the quantification procedure is demonstrated and corrected, revealing that the NP exhibits an incomplete coverage. The importance of sample preparation and cleaning as well as the influence of the support film is discussed. The analysis of the quantitative relationship between the cobalt / nickel content and the shape and intensity distribution of the O-K edge shows that the O-K ELNES signal is influenced by both the global and the local composition of the NP.

2. Materials and methods

2.1. Studied samples and their preparation

Table 1 lists the information and the naming convention of the five samples *Core, CS Co, CS Ni, CS Co2* and *CS Co+Ni* analyzed in this work. The synthesis of the *Core* and cobalt-containing samples is described elsewhere (Baaziz et al., 2014; Sartori et al., 2020,2021; Royer et al., 2022,2023; Makarchuk et al., 2025). The nickel-containing NPs were prepared in a similar way, which will be presented in detail in a separate article.

All NPs were dispersed in ethanol and drop-casted on standard holey-carbon TEM grids for STEM analysis. The *Core* NP sample was treated with a 14 s Ar+O$_2$ plasma cleaning step, all other samples were cleaned from ligands using activated carbon and ethanol as described in (Li et al., 2021).

2.2. Data acquisition

All data for this work were acquired using a probe-corrected Titan low-base (Thermo Fisher Scientific) equipped with high-brightness field emission gun (X-FEG), a monochromator and with a Gatan Imaging Filter (GIF) Tridiem 865 for EELS. High-angle annular dark-field (HAADF) STEM images were acquired at 300 kV with a convergence angle of 25 mrad and a collection angle of 48 mrad. EELS data were acquired *without* excitation of the monochromator and with a convergence angle α of 25 mrad and collection angles β above 52 mrad as noted in Table 1. With the exception of the *CS Co2* sample (300 kV), the gun was operated at 80 kV for the EELS acquisitions to decrease knock-on damage, to improve energy resolution, and because the cross sections of inelastic scattering increase. The beam current density was not measured, but the microscope was operated with the same illumination settings for all analyses (spot size 9, monochromator focus of $\approx$ 15). The estimated probe size for these conditions is approximately 0.2 nm and the pixel step sizes were 0.2 nm (*Core*), 0.5 nm (*CS Co2*) and 0.4 nm (remaining samples). The dwell times of the pixels were 0.3 s (*CS Co*) and 0.1 s (remaining samples).

The GIF EEL spectrometer was tuned prior to each session at the microscope and EELS spectrum images (SIs) were acquired using Digiscan (Digital Micrograph, Gatan) with drift-correction. The energy dispersion was set to 0.2 eV per channel for the *Core* and cobalt-containing NPs, as it allows to encompass the O-K (532 eV), Fe-L (708 eV) and Co-L (779 eV) ionization edges. The dispersion was increased to 0.3 eV per channel for the nickel-containing NPs to additionally record the Ni-L (855 eV) edge. The energy resolution (full width at half maximum of the zero-loss peak) was approximately 0.7 eV at 80 keV and 0.9 eV at 300 keV.

2.3. Data analysis

Data analysis was performed using a custom software (Hettler, 2024) and scripts based on Matlab (The Mathworks). The workflow for EELS data analysis consisted in an initial energy calibration (offset and dispersion) using the sum spectrum of each SI by setting the O-K pre-peak and Fe-L$_3$ peak positions to 532 eV and 710 eV, respectively. This calibration ensures comparability between the different samples. The dispersion after calibration was approximately 0.19 eV and 0.27 eV per channel for the two used hardware settings (0.2 and 0.3 eV per channel). A power-law background (BG) function was fitted to a specific energy window for each element and quantification was done by integrating the intensity in the BG-subtracted spectra in a window with a width of 30 eV. The positions of both windows are given in Table 2.

In addition to the 30 eV windows for compositional quantification, two smaller windows were set for the O-K edge to obtain ELNES information as described below. The windows with 3 eV width were placed around the O-K pre-peak and the following valley and the respective window positions are noted in Table 2 and are marked in Fig. 4f. In addition to the integration of energy windows, a single Gaussian function was fitted to the BG-subtracted Fe-L$_3$ peak (fit window from 707 to 713 eV).

All these analyses were performed on both raw and denoised datasets. For denoising, a principal-component analysis (PCA) was performed on each dataset and the number of components was set to a relatively large value (12). This large value was chosen as compromise between denoising and still having an accurate reproduction of the spectra on the single-pixel level, in close resemblance to the raw data. Although this large number leads to a small amount of noise, the overall noise is still considerably reduced compared to the raw data. The impact of PCA on the composition analysis and an exemplary comparison of raw and PCA-denoised spectra is shown in the supplementary material (Supp. Mat.), Section S1. Non-negative matrix factorization (NNMF) was tested and can give a good impression of the different phases, compositions, and linked spectral fingerprints present in the sample. However, it was discarded as it does not reproduce well the spectra on a single-

Table 2
Table with energy ranges for BG and quantification windows.

Edge	BG window / eV	Qu. window / eV
O-K	505–528	530–560
O-K pre-peak		530.4–533.4
O-K valley		533.4–536.4
Fe-L$_{2,3}$	670–703	705–735
Co-L$_{2,3}$	750–772	773–803
Ni-L$_{2,3}$	808–830	845–875

Table 1
List of investigated samples with designated name throughout this manuscript, literature references with details about synthesis and properties, cleaning methods as described in the text and acquisition conditions (high voltage (HV) and collection angle β). Convergence angle α was 25 mrad. The size (diameter) of the investigated NP, the average composition determined from the EELS-SI and the resulting δ of an assumed M$_3$O$_{4-\delta}$ structure with M=Fe,Co,Ni is given. Composition quantification of *CS Ni* and *CS Co+Ni* NPs was done considering the correction discussed in section 3.2.

Name	Ref.	Cleaning	HV kV	β mrad	Size nm	Composition [at%] O	Fe	Co	Ni	δ
Core	(Sartori et al., 2021)	14 s O$_2$ plasma	80	119	10	52.4	47.6	-	-	0.70
CS Co	(Royer et al., 2022,2023)	C+Eth	80	68	13	54.7	42	3.3	-	0.38
CS Ni	-	C+Eth	80	87	13	53.6	42.3	-	4.1	0.53
CS Co2	(Makarchuk et al., 2025)	C+Eth	300	52	17	56	35.7	8.3	-	0.18
CS Co+Ni	-	C+Eth	80	87	13	53.4	37.9	4.9	3.8	0.56

pixel basis needed for the quantitative ELNES analysis performed for this work. The results presented in the following were obtained from the PCA-denoised data.

The integration of intensity in the different edges for each point in the SI allows to generate intensity maps, which show the spatial distribution of the respective element within the SI. To generate a chemical map, the intensity maps of each element are rescaled to the interval [0,1] and a color is assigned to each element. The sum of the intensity maps then forms a RGB color image. In this work, the red color is assigned to oxygen, green to iron and blue to cobalt. Nickel is blue in *CS Ni* (total number of three elements) and yellow in the *CS Co+Ni* (total number of four elements). The chemical map only gives a qualitative description of the elemental distribution, showing where each element reaches its maximum (minimum) intensity. For a quantitative comparison in at%, the intensity is normalized by calculated theoretical cross sections σ (General oscillator strength (GOS)) (Egerton, 2011). As the collection angle β is at least more than two times larger than the convergence angle α for each dataset (Table 1), a correction for the incident beam convergence is not considered for the calculation of σ (see chapter 4.5.3 in (Egerton, 2011)).

3. Results and discussion

3.1. Overview of studied nanoparticles

An overview of the investigated NP systems is given in Figs. 1 and 2. Fig. 1 shows five exemplary HAADF-STEM images and the corresponding fast Fourier transforms (FFTs). The diameter of the investigated NPs is 10 nm for the *Core*, 13 nm for the *CS Co*, *CS Ni* and *CS Co+Ni* and 17 nm for the *CS Co2* NPs (Table 1). The images and FFTs reveal the excellent crystallinity of the NPs. All found reflections agree well with a magnetite spinel structure. A list of the major reflections found in the images and the identification of corresponding crystal planes is given in Section S2 of the Supp. Mat. Of interest is the appearance of weak kinematically forbidden [110] and [210] reflections for the *CS Co2* sample (marked by orange circles in the power spectrum of Fig. 1d), indicating that dynamical diffraction already occurs despite a thickness of below 20 nm. The relevant parameter for EELS is however the inelastic mean free path λ_{iMFP}, which is larger than 100 nm for iron or iron oxide (Egerton, 2011). The NP diameter thus corresponds to less than 20 % of the λ_{iMFP} and single inelastic scattering can be assumed.

From these images it is also seen that, with exception of the *CS Co2* sample, the NPs all exhibit a single phase and give no insight on a possible incorporation of Co or Ni in the magnetite matrix. Firstly, this is caused by the highly similar crystal structures of magnetite iron oxide and the corresponding ferrites. The lattice parameter of spinel nickel ($NiFe_2O_4$) (Wyckoff, 1931) and cobalt ($CoFe_2O_4$) (Ferreira et al., 2003) ferrites differs by less than 1 % from magnetite iron oxide and the difference is less than 2 % for Co_2FeO_4 (Ferreira et al., 2003), which makes a differentiation through EM imaging highly challenging. Secondly, the detection by contrast in the HAADF-STEM signal, which depends on the atomic number Z by approximately $Z^{1.7}$ is hindered by the small difference in atomic number between iron, cobalt and nickel, the relatively small amount of incorporated cobalt and nickel, as well as the non-homogeneous thickness across the spherical or slightly faceted NPs. Even in the case of the *CS Co2* NP (Fig. 1d), where two distinct phases with largely different composition are frequently found within a single NP, the HAADF-STEM image does not allow to deduce a chemical or structural difference between the two phases.

Despite showing largely different magnetic and catalytic properties (Sartori et al., 2021; Royer et al., 2022,2023; Makarchuk et al., 2025), HAADF-STEM imaging thus does not suffice to reveal the underlying differences in structure and composition and requires analytical techniques. Fig. 2a shows the sum spectra of EELS-SIs taken from NPs from each of the five samples. With exception of the *CS Co2* sample, the NPs investigated by EELS are different to the ones imaged in Fig. 1. Each of the sum spectra shows strong O-K and Fe-$L_{2,3}$ edges with only minor differences in the shape of these edges. The Co-$L_{2,3}$ is found in the cobalt-containing NPs with varying intensity and a Ni-$L_{2,3}$ edge is seen in the *CS Ni* and *CS Co+Ni* samples. The Ni-$L_{2,3}$ edge overlaps with the minor Fe-L_1 edge located at 846 eV, which is discussed in the following section.

The spectra shown in Fig. 2 have been normalized with respect to the intensity in the Fe-L_3 peak and a vertical offset has been added to improve visibility. The different slopes observed in the edge-free regions are mainly caused by the intensity in the C-K edge at 285 eV, which varies with the amount of sample support present within the EELS SI. For samples *Core*, *CS Co* and *CS Ni*, a NP suspended at the edge of a supporting film was selected for the EELS SI acquisition. In contrast, the selected *CS Co2* and *CS Co+Ni* NPs are suspended on the amorphous carbon (aC) film and a stronger background is present in the EEL spectra. The survey DF-STEM images of all samples are shown in Section S3 in the Supp. Mat.

The sum EEL spectra can be used to calculate the average composition of the investigated NPs. An oxygen content between 52 and 56 at% is found, leaving 48–44 at% for the metals (Table 1). Nickel and cobalt concentrations are below 5 at% for *CS Co* and *CS Ni* and below 10 at% for *CS Co2* and *CS Co+Ni*. From the determined composition, the δ in an assumed $M_3O_{4-\delta}$ (M=Fe,Co,Ni) stoichiometry is calculated (Table 1) and varies between 0.7 (*Core*) and 0.18 (*CS Co2*). These differences can be attributed to different effects. Firstly, for the *Core* sample, the high value of δ, which signifies a depletion of oxygen, is caused by the observed reduction of the NP at the surface (see section 3.3). A second possible influence is the amount of incorporated cobalt and nickel, which has an effect on the amount of oxygen in the iron oxide core (see section 3.4). Thirdly, the different high voltage (300 keV) used for the analysis of the *CS Co2* could also lead to differences in the quantification.

Fig. 2b-f shows the chemical maps of the EELS SI for the five studied samples. A spatially homogeneous composition is found for the *Core* sample, while a pronounced core-shell structure is observed for *CS Co*, *CS Ni* and *CS Co+Ni* samples with cobalt and nickel present predominantly or almost exclusively in a very narrow shell region. In case of the *CS Co2* NP, an increased cobalt content is found in the nano-grain seen in
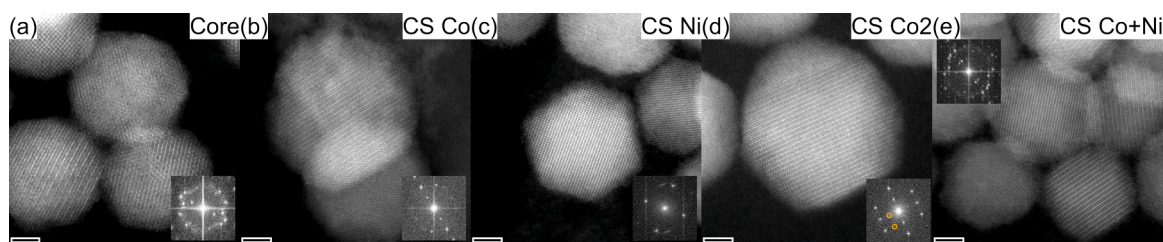

Fig. 1. HAADF STEM images of the investigated NP samples (a) pure magnetite (*Core*), (b) magnetite core with cobalt-rich shell (*CS Co*), (c) magnetite core with nickel-rich shell (*CS Ni*), (d) magnetite core with cobalt-rich islands (*CS Co2*) and (e) magnetite core with cobalt- and nickel-rich shell (*CS Co+Ni*). With exception of (d) *CS Co2*, these imaged NPs have not been used for the ELNES analysis below. Scale bars are (a) 2 nm and (b-e) 3 nm and FFTs have a width of 10.4 nm^{-1}.
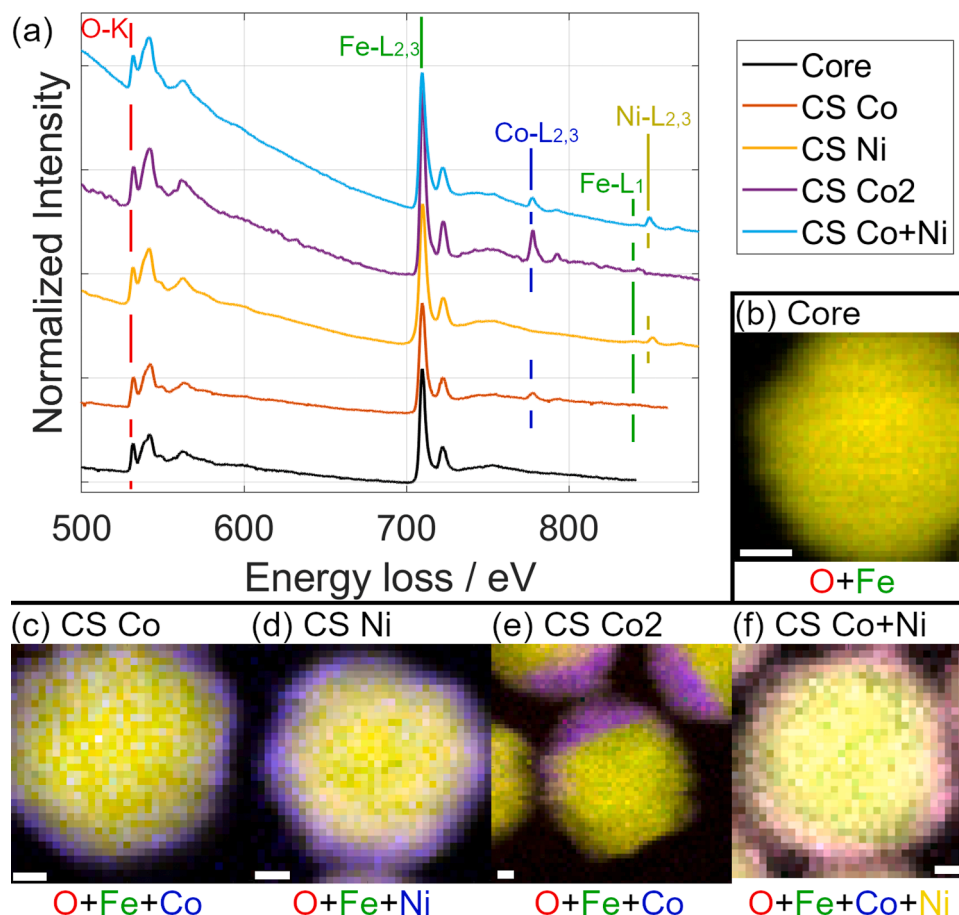
Fig. 2. (a) Sum spectra of the SIs for the 5 investigated samples with O-K, Fe-L, Co-L and Ni-L edges indicated. (b-f) Chemical maps of the (b) *Core*, (c) *CS Co*, (d) *CS Ni*, (e) *CS Co2* and (f) *CS Co+Ni* samples with the color assignation to elements as indicated. The composition correction discussed in section 3.2 has been considered for the shown chemical maps in (d,f). Scale bars are 2 nm.

the HAADF-STEM image (Fig. 1d), which adopts a $Co_{1.5}Fe_{1.5}O_4$ composition (Makarchuk et al., 2025).

3.2. Composition analysis

The quantification of the composition from the EELS data is straightforward for the samples with iron and cobalt presence only. However, the Ni-$L_{2,3}$ edge overlaps with the Fe-L_1 edge as visible from the sum spectra (Fig. 2a) and better seen from selected BG-subtracted spectra of the *CS Ni* NP (Fig. 3b). Fig. 3b shows a comparison of two BG-subtracted spectra taken from the core and shell region of the *CS Ni* NP as marked in Fig. 3e. The Fe-L_1 onset is found at 835 eV and the intensity in the edge, considering the energy window between approximately 835–845 eV, is increased in the core region (dashed line) with respect to the shell region (solid line). This is expected from the higher amount of Fe in the thicker core region of the NP. Stronger Ni-$L_{2,3}$ lines are found on top of the weak Fe-L_1 edge in the shell region, while they are absent in the core region, indicating a mere nickel presence in the shell. Although the Fe-L_1 edge is categorized as minor edge with reduced intensity, the strong presence of iron compared to nickel in the analyzed NPs causes a non-negligible contribution when quantifying the intensity in the Ni-$L_{2,3}$ edge. To remove the contribution of the Fe-L_1 edge to the Ni-$L_{2,3}$ edge, the intensity ratio between Fe-$L_{2,3}$ and Fe-L_1 was determined using experimental EEL spectra obtained from similar NP samples without nickel. Therefore, the intensities in the BG-subtracted Fe-$L_{2,3}$ (I ($Fe-L_{2,3}$)) and Fe-L_1 edges ($I(Fe-L_1)$) were integrated, selecting the BG and quantification windows used for the Ni-$L_{2,3}$ edge (Table 2) to calculate $I(Fe-L_1)$. The ratio $I(Fe-L_{2,3})/I(Fe-L_1)$ was determined to

1:0.04 ± 0.01 and the corrected intensity in the Ni-$L_{2,3}$ edge $I_{cor}(Ni-L_{2,3})$ was calculated from

$$I_{cor}(Ni-L_{2,3}) = I(Ni-L_{2,3}) - 0.04 \cdot I(Fe-L_{2,3}) \tag{1}$$

for each pixel (spectrum) of the EELS-SI. The impact is shown for a composition profile taken across the NP in Fig. 3c and for the chemical maps in Fig. 3d-f. While the change in oxygen and iron composition is relatively small, the nickel content in the core region is reduced to 0 at %. Considering the average nickel content in the entire NP, it decreases considerably from 6.4 at% to 3.8 at%.

This NP is an excellent example to illustrate the importance of the correction. The corrected nickel intensity map (Fig. 3f) shows that, in this projection, nickel is exclusively found at the surface of the NP and is absent in the core region. This implies that the shell of this NP is asymmetrical, adopting a torus-like shape as it is only covering the lateral sides of the NP in this particular orientation and leaving the top and bottom surfaces of the NP uncovered, at least partially. However, without the correction, a false nickel content is found in the core region as seen from both intensity map (Fig. 3e) and the composition line scan (Fig. 3c), which could lead to the erroneous assumption of a homogeneous shell. A possible reason for the asymmetrical coverage could be the preferential growth of the shell on specific facets of the NP. The faceted shape of the *CS Ni* NPs is clearly seen in the HAADF-STEM image in Fig. 1c.

The same correction procedure was performed for the *CS Co+Ni* sample and the results are shown in Section S4, Supp. Mat. The analysis of both nickel-containing NPs clearly emphasizes the importance of considering the overlap between Fe-L_1 and Ni-$L_{2,3}$ edge when
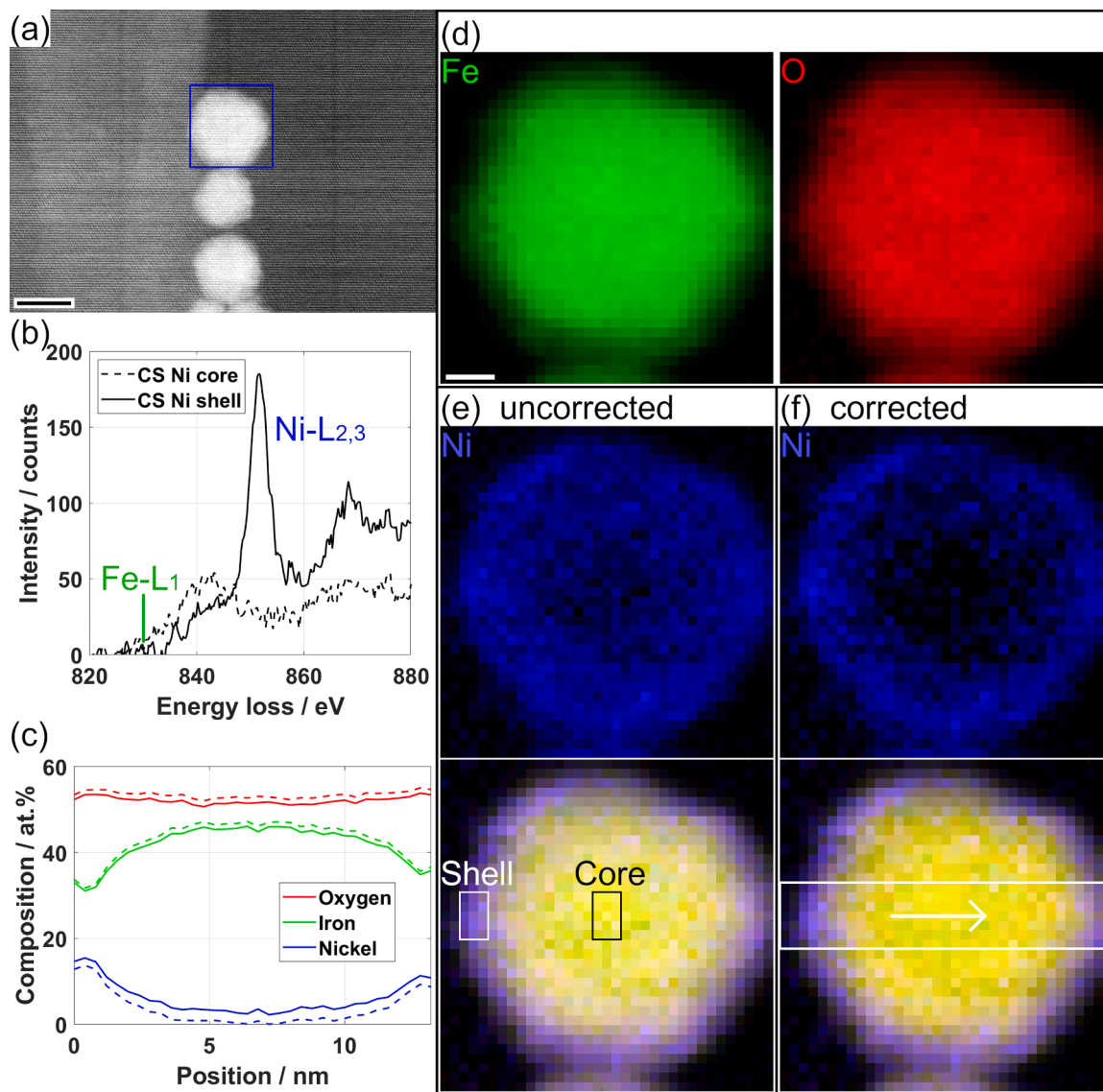
Fig. 3. Composition correction due to overlap between Fe-L$_1$ and Ni-L$_{2,3}$ edges. (a) Survey DF-STEM image of the investigated NP located at the edge of the film with the area for the EELS-SI acquisition marked. (b) Comparison of BG-subtracted Ni-L$_{2,3}$ edge taken from Ni-rich shell and core of the NP as marked in (e). (c) Composition profile across the NP as indicated in (f). Dashed lines correspond to the correction due to the edge overlap. (d) Iron and oxygen intensity maps. (e,f) Nickel intensity and chemical map (e) uncorrected and (f) corrected for edge overlap. Scale bars are (a) 9 nm and (d-f) 2 nm.

quantifying samples with high iron and low nickel content.

3.3. Reduction of magnetite Core NP

Fig. 4 shows the ELNES analysis of the *Core* sample, focusing on both O-K and Fe-L$_{2,3}$ edges. When looking at the chemical map of the *Core* NP (Fig. 4b), the NP seems to exhibit a fully homogeneous structure. Indeed, the composition profile taken across the NP (Fig. 4e) indicates a constant composition with only a barely detectable decrease by less than 1 at% in oxygen content at the surface of the NP. However, the comparison of the BG-subtracted and normalized O-K and Fe-L$_{2,3}$ edges taken from core and shell regions (Fig. 4f,g) reveals noticeable changes in the ELNES of both edges.

The spectra taken from the central region agree well with a magnetite iron oxide reference (Gloter et al., 2004; Chen et al., 2009; Ewels et al., 2016), for which the O-K edge exhibits a sharp pre-peak, which was centered at 532 eV for energy axis calibration, followed by a valley at 534.5 eV and a broader peak. The Fe-L$_{2,3}$ edge exhibits a sharp and intense L$_3$-peak centered at 708 eV (calibrated value) followed by a

smaller and broader L$_2$-peak. The difference in intensity in the L$_2$ peak to the reference can be attributed to the different employed BG-subtraction procedures (Chen et al., 2009). The L$_3$ peak position is directly related to the iron oxidation state in iron oxides and shifts to higher energies with increasing oxidation state (Garvie and Buseck, 1998). As magnetite iron oxide exhibits a mixture of Fe^{2+} and Fe^{3+} ions, the observed shift to lower energies at the NP surface compared to the center (Fig. 4e) indicates an increase in the Fe^{2+} species and thus a reduction at the surface. The partial reduction is as well reflected by the relatively low overall oxygen content (52.4 at%, Table 1) and the considerable deviation from a Fe$_3$O$_4$ stoichiometry. Fig. 4f shows that the O-K edge spectrum at the surface shows a strong increase in intensity of the valley at 534.5 eV and in the range of higher energies in comparison to the spectrum taken from the core region.

These two ELNES features, the shift of the Fe-L$_3$ peak and the redistribution of intensity in the O-K edge, indicate the surface reduction of the NP and can be used to visualize the spatial distribution of this reduction. Firstly, a map showing the Fe-L$_3$ peak position obtained from the fitting procedure (Fig. 4c) indicates a thin shell for which the peak is
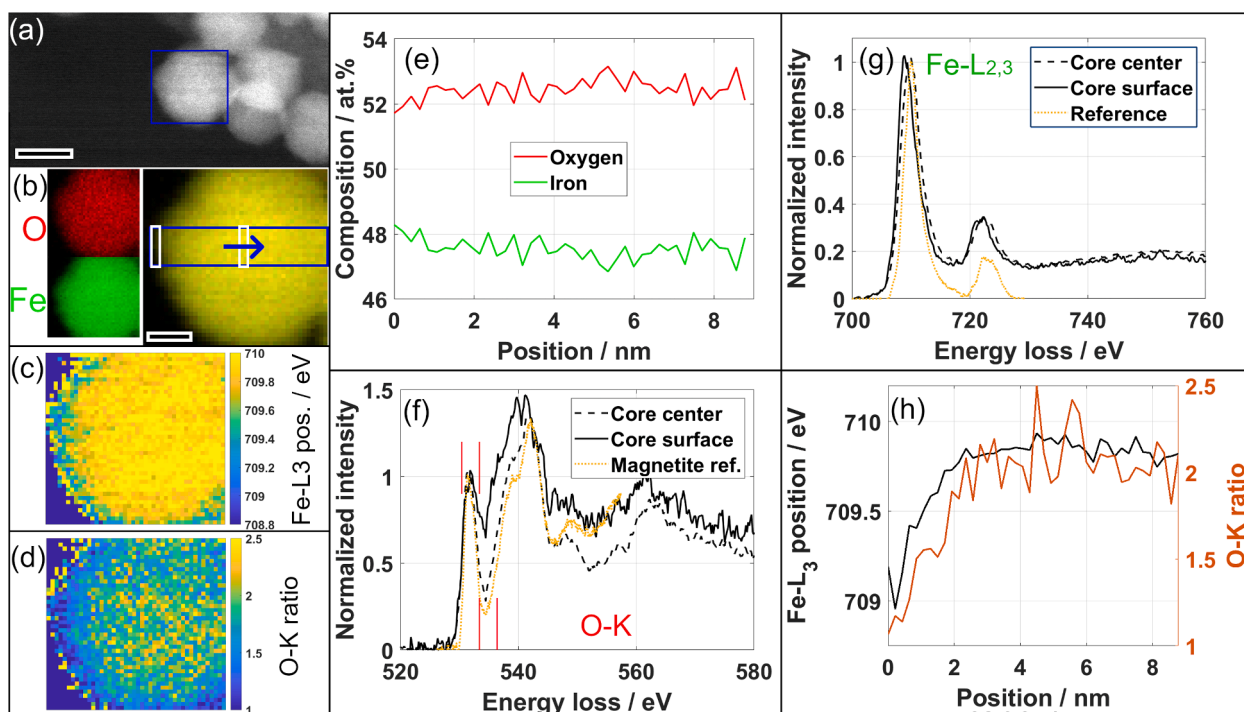
Fig. 4. ELNES analysis of the *Core* NP. (a) Survey image with EELS SI acquisition area marked. Scale bar is 6 nm. (b) Oxygen and iron intensity maps together with chemical map. Scale bar is 2 nm. (c,d) Maps of Fe-L_3 position and O-K ratio. Areas with minimum intensity in the Fe-L_3 and O-K edges have been set to the minimum value, respectively. (e) Composition line profile across the NP as indicated in the chemical map (b). (f,g) Comparison of (f) O-K and (g) Fe-$L_{2,3}$ edges taken from NP surface and NP center (marked by white frames in (b) with a magnetite reference spectrum. The spectra have been normalized with respect to the intensity in the peaks at 532 eV and 710 eV, respectively. (h) Line profile of Fe-L_3 position and O-K ratio.

shifted. Secondly, the intensity ratio between pre-peak and following valley in the O-K edge (designated as O-K ratio in the following) is calculated with the values of the energy ranges given in Table 1 and visualized by vertical red lines in Fig. 4f. In the corresponding map (Fig. 4d), a similar distribution is seen, with a slightly larger thickness of the shell. The plot of both O-K ratio and Fe-L_3 peak position taken from a line profile across the NP (Fig. 4h, marked in 4b) shows that both features are linked to each other.

Magnetite iron oxide NPs are stable at ambient conditions and a surface reduction does not occur upon contact with air or during O_2 plasma cleaning, suggesting that the observed surface reduction is caused by electron beam damage. As such a reduction has not been observed in similar studies of samples after incorporation of a ligand cleaning method (Li et al., 2021), the reduction process is believed to be linked to or at least favored by a chemical reaction with remaining surfactants and organic residues on the NP surface that have not been fully removed by the plasma cleaning process. A possible reaction mechanism could be the breakage of hydrocarbon bonds in the surfactant molecules by radiolysis. This leads to atoms with dangling bonds, which could then react with the oxygen atoms of the magnetite NP. This process adds to the direct reduction of the iron oxide NPs by knock-on damage, leading to the observed increased damage compared to NPs without surface ligands present. These results stress the importance of clean sample preparation. All other NP samples have been cleaned using the method described in (Li et al., 2021) (see Table 1) and a similar reduction could not be observed for these samples.

3.4. O-K edge ELNES with incorporated cobalt and nickel

Fig. 5 shows the ELNES analysis of the *CS Co* NP. The composition analysis revealed a very thin shell with maximum cobalt contents of 10–15 at% at the very edge of the NP (Fig. 5b) (Royer et al., 2023). Due to the low content and the small thickness at the very edge, there is little intensity in the Co-$L_{2,3}$ edge and it is challenging to reveal smaller

differences of the cobalt content within the NP, making an alternative means of detection desirable. Fig. 5d shows a comparison of the Co-$L_{2,3}$ spectrum for the core (dashed line) and shell (solid) regions, which have been marked in Fig. 5b. The increase in intensity in the shell region is clearly seen, which agrees with the core-shell structure. Fig. 5e depicts the corresponding normalized O-K edge spectra in comparison with the magnetite reference (orange dotted line) and a spectrum taken from a Co-rich grain of the *CS Co2* NP (blue dotted line). The comparison reveals that the intensity in the valley following the pre-peak increases with the amount of cobalt incorporated in the magnetite NP: It shows a smaller increase in the *CS Co* core region (2 at%), which is more pronounced in the shell region (7.8 at%) and strongly increased for the *CS Co2* shell (23.1 at%). As no detectable change can be observed in the Fe-$L_{2,3}$ edge of the *CS Co* NP that could indicate a significant reduction (Fig. 5f), the modification of the O-K edge is attributed to the presence of cobalt.

The observed trend in the O-K edge signifies that the O-K ratio as described in the previous section is sensitive to the cobalt content in the magnetite NP. Indeed, when creating a map of the O-K ratio for the *CS Co* NP (Fig. 5c), it clearly correlates with the Co distribution and confirms the core-shell structure of the NP. Furthermore, it highlights that the upper part of the NP contains a larger region with increased cobalt content, which is hard to see in the chemical map in Fig. 5b. The correlation between cobalt content and O-K ratio is also seen in a line profile taken across the NP as shown in Fig. 5g and marked in Fig. 5b. The small increase of cobalt content at the shell translates in a clear drop of the O-K ratio. The quantitative relationship will be discussed in more detail below.

A similar analysis performed on the nickel-containing *CS Ni* NP is shown in Fig. 6a-c. The selected regions of core and shell spectra (Fig. 6a,b) and the position of the line profile (Fig. 6c) are marked in Fig. 3. Again, the intensity in the valley of the O-K pre-peak increases in the shell region (solid black line in Fig. 6a, 12 at% nickel), when compared with the core region (dashed, only 0.4 at%), which exhibits a
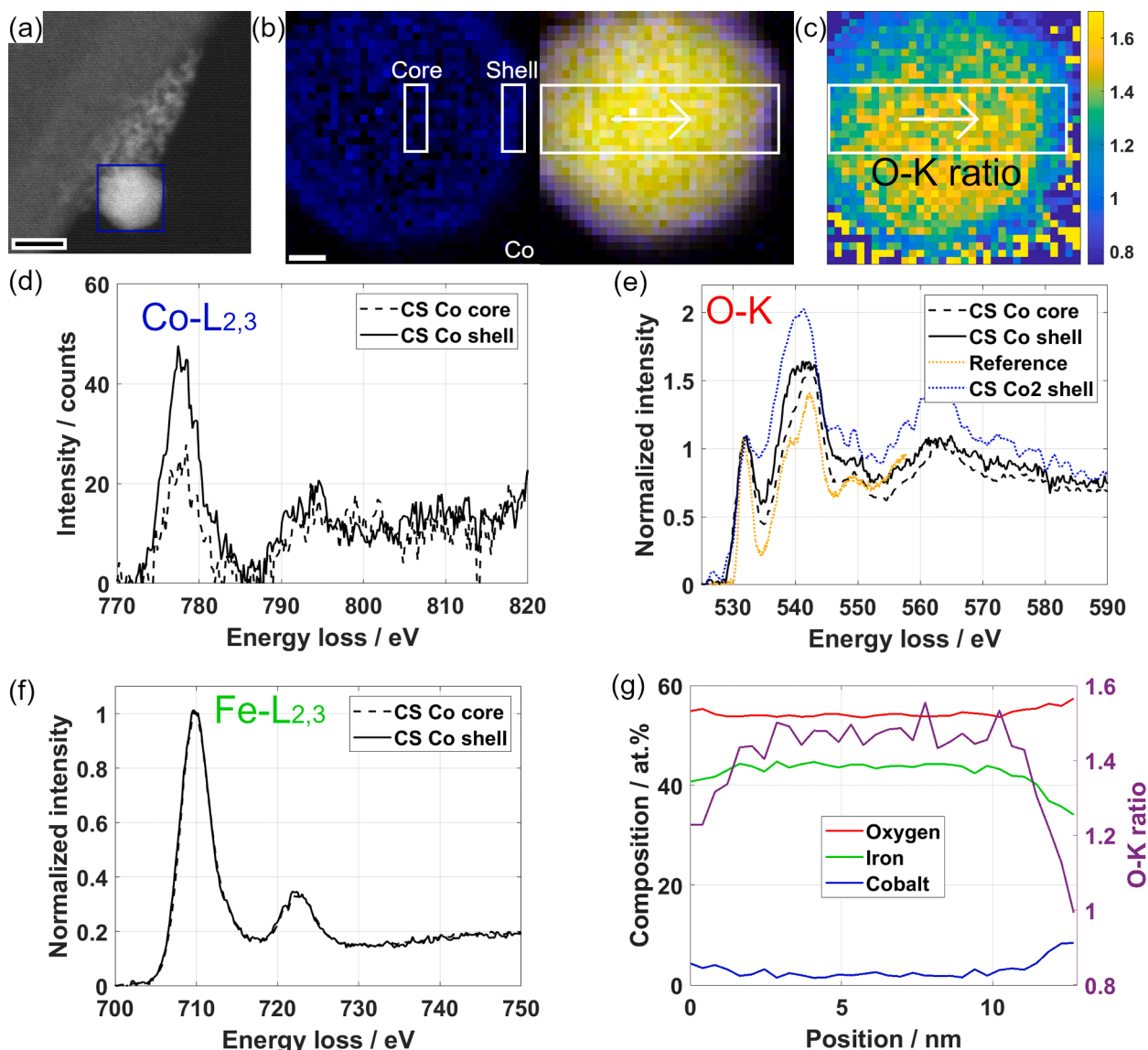
Fig. 5. Analysis of the *CS Co* NP. (a) Survey DF-STEM image with area for EELS SI marked. (b) Cobalt intensity map with areas for core and shell regions and chemical map with position of line profile shown in (g). (c) O-K ratio map. (d-f) Comparison of core (dashed black line, cobalt content 2 at%) and shell (solid black, 7.8 at%) regions of the *CS Co* NP for (d) the Co-L$_{2,3}$, (e) the O-K and (f) the Fe-L$_{2,3}$ edges. A magnetite reference spectrum and a spectrum taken from the cobalt-rich shell (23.1 at%) of the *CS Co2* NP have been added to the O-K spectra shown in (e). The O-K and Fe-L$_{2,3}$ spectra have been normalized with respect to the intensity in the peaks at 532 eV and 710 eV, respectively. (g) Line profile across the NP comparing compostion with O-K ratio (purple line). Scale bars are (a) 10 nm and (b, c) 2 nm.

strongly reduced nickel content. Notably, the core region exhibits an already strongly increased intensity when compared to a magnetite reference spectrum (orange dotted line), despite the negligible nickel content. The Fe-L$_{2,3}$ peak shows no detectable shift between core and shell regions (Fig. 6b). The line profile showing composition and O-K ratio (Fig. 6c) reveals that the relationship between nickel content and O-K ratio follows the same trend, that is a decreasing O-K ratio with increasing nickel content, which is however less pronounced when compared to cobalt incorporation (Fig. 5g).

Fig. 6d-f shows the same analysis performed on the *CS Co+Ni* NP (see chemical maps in Fig. 2f and Section S4, Supp. Mat.) and confirms the observations of both *CS Co* and *CS Ni* samples: The O-K ratio drops with increasing cobalt and nickel content (Fig. 6d+f), while the Fe-L$_{2,3}$ edge shows only a minimum change. This NP, which was fully suspended on a supporting carbon film, serves to show the respective impact on the EELS analysis. Therefore, an O-K spectrum was obtained from a substrate region without NP and subtracted from the O-K spectra before

integration (Section S5, Supp. Mat.). Fig. 6f compares the line profiles of composition and O-K ratio obtained with (dashed lines) and without (solid lines) correction of the substrate contribution. The correction leads to a reduction of the oxygen content by less than 2 % at the NP surface and less than 0.5 % in the core region. The total metal composition is increased by the same amount and the O-K ratio is shifted by an almost constant offset. The small change can be neglected for qualitative analyses but the contribution of the supporting substrate needs to be considered when doing precise measurements or ELNES analyses and NPs located at the edge of the supporting film should be preferred.

3.5. Toward an absolute quantitative relationship between O-K ratio and cobalt / nickel content

The conducted analyses show that for each of the NPs, the O-K ratio decreases with a local increase in the cobalt and/or nickel content. The data from the different NPs can be used to obtain a quantitative
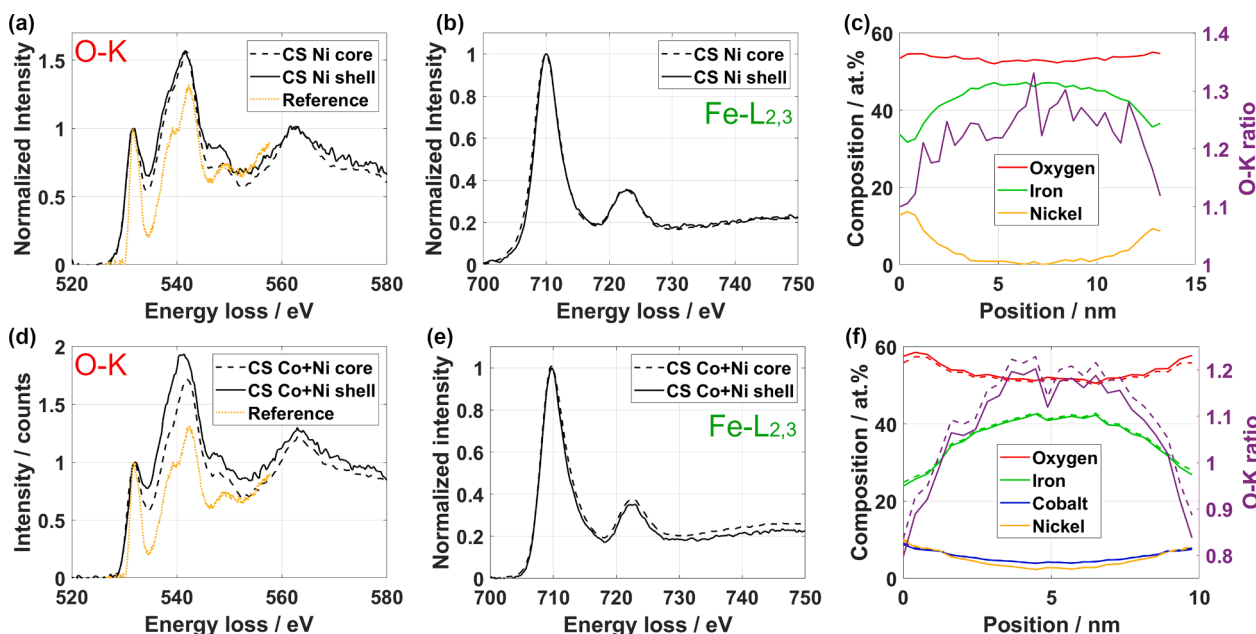
Fig. 6. Analysis of the (a-c) *CS Ni* and (d-f) *CS Co+Ni* NPs showing a comparison of the (a,d) O-K and (b,e) Fe-L$_{2,3}$ edges from core and shell regions and a (c,f) a comparison of composition and O-K ratio. A magnetite reference spectrum has been added to the O-K edge graph (a,d). The nickel content in the shell and core of the *CS Ni* NP was 12 at% and 0.4 at%, respectively. The cobalt / nickel content of the *CS Co+Ni* NP was 3.3/1.4 at% in the shell and 7.8/8.2 at% in the core, respectively. The dashed line in (f) represents data were the O-K background signal from the supporting aC film has been considered.

relationship between the O-K ratio and the cobalt / nickel content. Fig. 7a and b show scatter plots of this relationship for the cobalt-containing NPs (Fig. 7a) and the *CS Ni* NP (Fig. 7b). Two similar EELS-SIs of additional NPs of the *CS Co* and *CS Ni* samples (not shown) have been included in these scatter plots, where one plotted circle represents a single spectrum of the EELS-SIs. The color saturation has been scaled with the overall intensity in the O-K edge of that pixel, thus giving an indication for the noise. Data points with relative oxygen intensities below 7 % of the maximum oxygen intensity in the EELS-SI have been discarded. While strongly colored data points are clouded around a rather narrow range and follow a trend, colorless points exhibit a larger broadening.

Fig. 7a shows the relationship for the *CS Co* and *CS Co2* NPs, which cover two different ranges of cobalt contents. The data of the *CS Co* NP is located mostly at contents below 5 at% due to the low incorporated amounts. The *CS Co2* NP shows two strong clouds, one located at low contents caused by the small amount of cobalt incorporated in the core of the NP and a second at contents between 20 and 25 at% originating from the cobalt-rich nano-grains seen in these NPs. In between, the density of points is reduced and considerably broadened due to a larger number of weakly colored points stemming from the very edge of the NP with low intensity in the O-K edge.

The data of both NPs on their own follow a rather straight line, but a clear difference is observed between both samples at low cobalt contents with the O-K ratio being considerably larger for the *CS Co* NP. A small part of this difference is explained by the aC film background present in the *CS Co2* NP, which can lead to a small decrease of the O-K ratio (Fig. 6f). However, this contribution only amounts up to a maximum of 0.03, not enough to explain the full difference between *CS Co* and *CS Co2*.

A possible explanation could be that the large overall cobalt content caused by the presence of areas with high cobalt content at the surface of the *CS Co2* NP could have an impact on the ELNES signal of the iron oxide core. Oxygen vacancies are a common point defect in magnetite iron oxide and are known to diffuse. Due to the small size of the NPs, it is highly probable that oxygen atoms can move to the cobalt- (or nickel-) rich surface and lead to an oxygen depletion in the remaining iron oxide core area due to a possible preferred bonding to cobalt (or nickel) ions. Indeed, such a depletion of oxygen is observed in all the analyzed core-shell NPs as observed from the composition line profiles (*CS Co* in Fig. 5g, *CS Ni* in Fig. 6c and *CS Co+Ni* in Fig. 6f). The depletion increases with the amount of implemented cobalt and nickel, reaching more than 5 at% difference between core and shell in case of the *CS Co+Ni* NP (Fig. 6f). This suggests that there is a higher density of oxygen vacancies
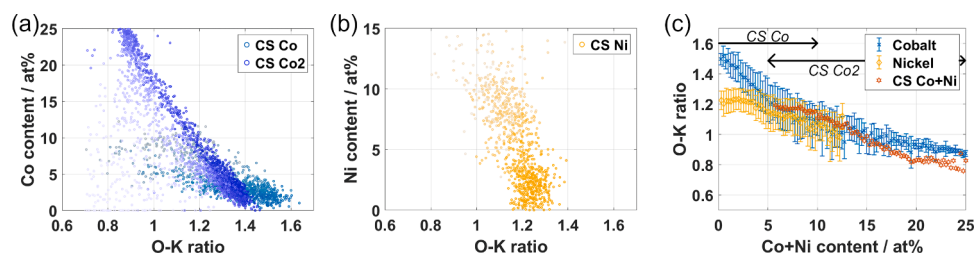

Fig. 7. Quantitative comparison of cobalt and nickel content with the O-K ratio. (a) Scatter plot of cobalt content over O-K ratio for the *CS Co* (light blue) and *CS Co2* (dark blue) samples. (b) Scatter plot of nickel content over O-K ratio for the *CS Ni* sample. Color saturation in (a,b) is scaled with the intensity in the O-K edge in the respective pixel. (c) Plot of the O-K ratio over the combined cobalt and nickel content for the cobalt (blue) and nickel (yellow) containing NPs and the *CS Co+Ni* NP (orange hexagons). The range of cobalt contents, for which the data of the *CS Co* and *CS Co2* samples was considered, is marked. Error bars for the *CS Co+Ni* NP have been neglected for better visibility.

in the core region, which increases with the amount of cobalt and nickel incorporated in the shell. Although the exact chemical and atomistic configuration is difficult to asses, it can be seen as an effective reduction of the core. As seen in the analysis of the *Core* NP, the O-K ratio decreases strongly upon reduction (Fig. 4), which could explain the lower O-K ratio for the *CS Co2* NP due to an effective reduction of the iron oxide in the core region. A similar effect could be responsible for the shift to lower O-K ratios in the *CS Ni* NP already for low nickel contents (Fig. 6a, c and Fig. 7b), when compared to pure magnetite iron oxide. The relatively large modification suggests that the effect is stronger for nickel.

The data have been combined to extract an average value for the O-K ratio in dependence of the cobalt / nickel content, which is plotted in Fig. 7c. It is clearly visible that the O-K ratio decreases with increasing cobalt (blue crosses) and nickel (yellow diamonds) content. The stronger dependence of the O-K ratio on the cobalt content compared to the nickel content seen in the line profiles is confirmed. In addition, orange hexagons represent the data from the *CS Co+Ni* NP. For the cobalt curve, only the data of the *CS Co* NPs was considered for contents < 5 at%. The error bars reflect the statistical variation of the O-K ratio for the given cobalt / nickel content.

The observations indicate that the O-K ratio depends both on the local and global composition of the NP, which hinders the establishment of an absolute quantitative link between O-K ratio and cobalt / nickel content in magnetite iron oxide. Nevertheless, the relative change of the O-K ratio is a useful quantity to locally assess the presence of cobalt and nickel within individual magnetite-based core-shell NPs. Further experimental data with higher energy resolution, on an absolute energy scale and ideally acquired with direct electron detectors to reduce the noise are required to disentangle these dependencies.

4. Conclusion

The STEM-EELS and ELNES analysis performed in this work illustrates the potential of the technique to analyze composition and chemistry of core-shell NPs based on magnetite iron oxide with high spatial resolution. While chemical maps give a good impression of the spatial elemental distribution, more detailed analyses are required to illustrate smaller compositional and chemical modifications within the NPs. The importance of considering the overlap between the Fe-L$_1$ and Ni-L$_{2,3}$ edges has been demonstrated. A surface reduction of pure magnetite NPs is observed for NPs that have not been fully cleaned of surface ligands. An intensity ratio between two narrow energy windows within the O-K edge was shown to be directly linked to the local cobalt / nickel content in the analyzed NPs. This relationship can be used to visualize spatially-varying chemical modifications within the NP. The analysis of the quantitative relationship between this O-K ratio and the incorporated amounts of cobalt / nickel suggests that it not only depends on the local composition, but as well on the global amount of incorporated cobalt and nickel.

CRediT authorship contribution statement

Raul Arenal: Writing – review & editing, Project administration, Funding acquisition. **Simon Hettler:** Writing – review & editing, Writing – original draft, Visualization, Validation, Software, Methodology, Investigation, Formal analysis, Data curation, Conceptualization.

Declaration of Competing Interest

The authors declare that they have no known competing financial interests or personal relationships that could have appeared to influence the work reported in this paper.

Data Availability

Data is available under https://doi.org/10.5281/zenodo.13913065.

Appendix A. Supporting information

Supplementary data associated with this article can be found in the online version at doi:10.1016/j.micron.2025.103858.

References

Ajinkya, N., Yu, X., Kaithal, P., Luo, H., Somani, P., Ramakrishna, S., 2020. Magnetic iron oxide nanoparticle (ionp) synthesis to applications: present and future. Materials 13 (20), 4644. https://doi.org/10.3390/ma13204644.

van Aken, P.A., Liebscher, B., Styrsa, V.J., 1998. Quantitative determination of iron oxidation states in minerals using fe l 2,3 -edge electron energy-loss near-edge structure spectroscopy. Phys. Chem. Miner. 25 (5), 323–327. https://doi.org/10.1007/s002690050122.

Baaziz, W., Pichon, B.P., Fleutot, S., Liu, Y., Lefevre, C., Greneche, J.-M., Toumi, M., Mhiri, T., Begin-Colin, S., 2014. Magnetic iron oxide nanoparticles: reproducible tuning of the size and nanosized-dependent composition, defects, and spin canting. J. Phys. Chem. C 118 (7), 3795–3810. https://doi.org/10.1021/jp411481p.

Barreca, D., Gasparotto, A., Lebedev, O.I., Maccato, C., Pozza, A., Tondello, E., Turner, S., Van Tendeloo, G., 2010. Controlled vapor-phase synthesis of cobalt oxide nanomaterials with tuned composition and spatial organization. CrystEngComm 12 (7), 2185. https://doi.org/10.1039/b926368n.

Blanco-Portals, J., Peiró, F., Estradé, S., 2021. Strategies for eels data analysis. introducing umap and hdbscan for dimensionality reduction and clustering. Microsc. Microanal. 28 (1), 109–122. https://doi.org/10.1017/s1431927621013696.

Bustamante Torres, M., Romero Fierro, D., Estrella-Nuñez, J., Arcentales-Vera, B., Chichande-Proaño, E., Bucio, E., 2022. Polymeric composite of magnetite iron oxide nanoparticles and their application in biomedicine: a review. Polymers 14 (4), 752. https://doi.org/10.3390/polym14040752.

Chen, S.-Y., Gloter, A., Zobelli, A., Wang, L., Chen, C.-H., Colliex, C., 2009. Electron energy loss spectroscopy andab initioinvestigation of iron oxide nanomaterials grown by a hydrothermal process. Phys. Rev. B 79 (10), 104103. https://doi.org/10.1103/physrevb.79.104103.

Egerton, R.F., 2011. Electron Energy-Loss Spectroscopy in the Electron Microscope, 3rd Edition. Springer Science+Business Media LLC, Boston, MA. https://doi.org/10.1007/978-1-4419-9583-4.

Estrader, M., López-Ortega, A., Golosovsky, I.V., Estradé, S., Roca, A.G., Salazar-Alvarez, G., López-Conesa, L., Tobia, D., Winkler, E., Ardisson, J.D., Macedo, W.A.A., Morphis, A., Vasilakaki, M., Trohidou, K.N., Gukasov, A., Mirebeau, I., Makarova, O. L., Zysler, R.D., Peiró, F., Baró, M.D., Bergström, L., Nogués, J., 2015. Origin of the large dispersion of magnetic properties in nanostructured oxides: Fexo/fe3o4 nanoparticles as a case study. Nanoscale 7 (7), 3002–3015. https://doi.org/10.1039/c4nr06351a.

Ewels, P., Sikora, T., Serin, V., Ewels, C.P., Lajaunie, L., 2016. A complete overhaul of the electron energy-loss spectroscopy and x-ray absorption spectroscopy database: eelsdb.eu. Microsc. Microanal. 22, 717–724. https://doi.org/10.1017/S1431927616000179.

Ferreira, T., Waerenborgh, J., Mendonça, M., Nunes, M., Costa, F., 2003. Structural and morphological characterization of feco2o4 and cofe2o4 spinels prepared by a coprecipitation method. Solid State Sci. 5 (2), 383–392. https://doi.org/10.1016/s1293-2558(03)00011-6.

Garvie, L.A.J., Buseck, P.R., 1998. Ratios of ferrous to ferric iron from nanometre-sized areas in minerals. Nature 396 (6712), 667–670. https://doi.org/10.1038/25334.

Gavrilov-Isaac, V., Neveu, S., Dupuis, V., Taverna, D., Gloter, A., Cabuil, V., 2015. Synthesis of trimagnetic multishell mnfe2o4@cofe2o4@nife2o4 nanoparticles. Small 11 (22), 2614–2618. https://doi.org/10.1002/smll.201402845.

Gloter, A., Zbinden, M., Guyot, F., Gaill, F., Colliex, C., 2004. Tem-eels study of natural ferrihydrite from geological-biological interactions in hydrothermal systems. Earth Planet. Sci. Lett. 222 (3-4), 947–957. https://doi.org/10.1016/j.epsl.2004.03.040.

S. Hettler, Temsuite - a matlab-based software platform for tem data analysis, In: European Microscopy Conference, 2024.

Knappett, B.R., Abdulkin, P., Ringe, E., Jefferson, D.A., Lozano-Perez, S., Rojas, T.C., Fernández, A., Wheatley, A.E.H., 2013. Characterisation of co@fe3o4 core@shell nanoparticles using advanced electron microscopy. Nanoscale 5 (13), 5765. https://doi.org/10.1039/c3nr33789h.

Li, C., Tardajos, A.P., Wang, D., Choukroun, D., Van Daele, K., Breugelmans, T., Bals, S., 2021. A simple method to clean ligand contamination on tem grids. Ultramicroscopy 221, 113195. https://doi.org/10.1016/j.ultramic.2020.113195.

Lima, E., Winkler, E.L., Tobia, D., Troiani, H.E., Zysler, R.D., Agostinelli, E., Fiorani, D., 2012. Bimagnetic coo core/cofe2o4 shell nanoparticles: synthesis and magnetic properties. Chem. Mater. 24 (3), 512–516. https://doi.org/10.1021/cm2028959.

Lin, F., Nordlund, D., Weng, T.-C., Zhu, Y., Ban, C., Richards, R.M., Xin, H.L., 2025. Phase evolution for conversion reaction electrodes in lithium-ion batteries. Nat. Commun. 5 (1). https://doi.org/10.1038/ncomms4358.

López-Ortega, A., Estrader, M., Salazar-Alvarez, G., Estradé, S., Golosovsky, I.V., Dumas, R.K., Keavney, D.J., Vasilakaki, M., Trohidou, K.N., Sort, J., Peiró, F., Suriñach, S., Baró, M.D., Nogués, J., 2012. Strongly exchange coupled inverse ferrimagnetic soft@hard, mnxfe3-xo4@fexmn3-xo4, core@shell heterostructured nanoparticles. Nanoscale 4 (16), 5138. https://doi.org/10.1039/c2nr30986f.

López-Ortega, A., Estrader, M., Salazar-Alvarez, G., Roca, A.G., Nogués, J., 2015. Applications of exchange coupled bi-magnetic hard@soft and soft@hard magnetic core@shell nanoparticles. Phys. Rep. 553, 1–32. https://doi.org/10.1016/j.physrep.2014.09.007.

López-Ortega, A., Lottini, E., Bertoni, G., de Julián Fernández, C., Sangregorio, C., 2017. Topotaxial phase transformation in cobalt doped iron oxide core/shell hard magnetic nanoparticles. Chem. Mater. 29 (3), 1279–1289. https://doi.org/10.1021/acs.chemmater.6b04768.

Makarchuk, I., Rotonnelli, B., Royer, L., Hettler, S., Gallet, J.-J., Bournel, F., Guehl, J., Brige, A., Zitolo, A., Kéranguéven, G., Bonnefont, A., Arenal, R., Savinova, E., Asset, T., Pichon, B.P., 2025. Effect of shell thickness on the oxygen evolution activity of core@shell fe3o4@cofe2o4 nanoparticles. Chem. Mater. 37 (3), 833–844. https://doi.org/10.1021/acs.chemmater.4c01784.

Mitterbauer, C., Kothleitner, G., Grogger, W., Zandbergen, H., Freitag, B., Tiemeijer, P., Hofer, F., 2003. Electron energy-loss near-edge structures of 3d transition metal oxides recorded at high-energy resolution. Ultramicroscopy 96 (3-4), 469–480. https://doi.org/10.1016/s0304-3991(03)00109-8.

Nuñez, J.M., Hettler, S., Lima Jr, E., Goya, G.F., Arenal, R., Zysler, R.D., Aguirre, M.H., Winkler, E.L., 2022. Onion-like fe3o4/mgo/cofe2o4 magnetic nanoparticles: new ways to control magnetic coupling between soft and hard magnetic phases. J. Mater. Chem. C. 10 (41), 15339–15352. https://doi.org/10.1039/d2tc03144b.

Pate, C.M., Hart, J.L., Taheri, M.L., 2025. Rapideels: machine learning for denoising and classification in rapid acquisition electron energy loss spectroscopy. Sci. Rep. 11 (1). https://doi.org/10.1038/s41598-021-97668-8.

Potapov, P.L., Kulkova, S.E., Schryvers, D., Verbeeck, J., 2001. Structural and chemical effects oneelsl3,2ionization edges in ni-based intermetallic compounds. Phys. Rev. B 64 (18), 184110. https://doi.org/10.1103/physrevb.64.184110.

Roldan, M.A., Mayence, A., López-Ortega, A., Ishikawa, R., Salafranca, J., Estrader, M., Salazar-Alvarez, G., Dolors Baró, M., Nogués, J., Pennycook, S.J., Varela, M., 2021. Probing the meta-stability of oxide core/shell nanoparticle systems at atomic resolution. Chem. Eng. J. 405, 126820. https://doi.org/10.1016/j.cej.2020.126820.

Royer, L., Bonnefont, A., Asset, T., Rotonnelli, B., Velasco-Vélez, J.-J., Holdcroft, S., Hettler, S., Arenal, R., Pichon, B., Savinova, E., 2022. Cooperative redox transitions drive electrocatalysis of the oxygen evolution reaction on cobalt-iron core-shell nanoparticles. ACS Catal. 13 (1), 280–286. https://doi.org/10.1021/acscatal.2c04512.

Royer, L., Makarchuk, I., Hettler, S., Arenal, R., Asset, T., Rotonnelli, B., Bonnefont, A., Savinova, E., Pichon, B.P., 2023. Core-shell fe3o4@cofe2o4 nanoparticles as high-performance anode catalysts for enhanced oxygen evolution reaction. Sustain. Energy Fuels 7 (14), 3239–3243. https://doi.org/10.1039/d3se00130j.

Sartori, K., Gailly, D., Bouillet, C., Grenéche, J.-M., Dueñas-Ramirez, P., Begin-Colin, S., Choueikani, F., Pichon, B.P., 2020. Increasing the size of fe3o4 nanoparticles by performing a multistep seed-mediated growth approach. Cryst. Growth Des. 20 (3), 1572–1582. https://doi.org/10.1021/acs.cgd.9b01300.

Sartori, K., Musat, A., Choueikani, F., Grenéche, J.-M., Hettler, S., Bencok, P., Begin-Colin, S., Steadman, P., Arenal, R., Pichon, B.P., 2021. A detailed investigation of the onion structure of exchanged coupled magnetic fe3o4@cofe2o4@fe3o4 nanoparticles. ACS Appl. Mater. Interfaces 13 (14), 16784–16800. https://doi.org/10.1021/acsami.0c18310.

Tan, H., Verbeeck, J., Abakumov, A., Van Tendeloo, G., 2012. Oxidation state and chemical shift investigation in transition metal oxides by eels. Ultramicroscopy 116, 24–33. https://doi.org/10.1016/j.ultramic.2012.03.002.

Tartaj, P., Morales, M.P., Gonzalez-Carreño, T., Veintemillas-Verdaguer, S., Serna, C.J., 2011. The iron oxides strike back: From biomedical applications to energy storage devices and photoelectrochemical water splitting. Adv. Mater. 23 (44), 5243–5249. https://doi.org/10.1002/adma.201101368.

Torruella, P., Arenal, R., de la Peña, F., Saghi, Z., Yedra, L., Eljarrat, A., López-Conesa, L., Estrader, M., López-Ortega, A., Salazar-Alvarez, G., Nogués, J., Ducati, C., Midgley, P.A., Peiró, F., Estradé, S., 2016. 3d visualization of the iron oxidation state in feo/fe3o4core-shell nanocubes from electron energy loss tomography. Nano Lett. 16 (8), 5068–5073. https://doi.org/10.1021/acs.nanolett.6b01922.

Turner, S., Lazar, S., Freitag, B., Egoavil, R., Verbeeck, J., Put, S., Strauven, Y., Tendeloo, G.Van, 2011. High resolution mapping of surface reduction in ceria nanoparticles. Nanoscale 3 (8), 3385. https://doi.org/10.1039/c1nr10510h.

Wallyn, J., Anton, N., Vandamme, T.F., 2019. Synthesis, principles, and properties of magnetite nanoparticles for in vivo imaging applications—a review. Pharmaceutics 11 (11), 601. https://doi.org/10.3390/pharmaceutics11110601.

Wyckoff, R., 1931. The Structure of Crystals, 2nd edition. The Chemical Catalog Company. inc.

Yedra, L., Xuriguera, E., Estrader, M., López-Ortega, A., Baró, M.D., Nogués, J., Roldan, M., Varela, M., Estradé, S., Peiró, F., 2014. Oxide wizard: an eels application to characterize the white lines of transition metal edges. Microsc. Microanal. 20 (3), 698–705. https://doi.org/10.1017/s1431927614000440.